











# In vivo bone marrow microenvironment siRNA delivery using lipid–polymer nanoparticles for multiple myeloma therapy

Pedro P. G. Guimarães<sup>a,b,1</sup> , Christian G. Figueroa-Espada<sup>a,1</sup> , Rachel S. Riley<sup>a,c</sup>, Ningqiang Gong<sup>a</sup>, Lulu Xue<sup>a</sup> , Tomasz Sewastianik<sup>d,e</sup> , Peter S. Dennis<sup>d</sup>, Claudia Loebelf<sup>f</sup>, Amanda Chung<sup>g</sup>, Sarah J. Shepherd<sup>g</sup>, Rebecca M. Haley<sup>a</sup> , Alex G. Hamilton<sup>a</sup> , Rakan El-Mayta<sup>a</sup> , Karin Wang<sup>h</sup>, Robert Langer<sup>g,i,j,k</sup> , Daniel G. Anderson<sup>g,i,j,k</sup>, Ruben D. Carrasco<sup>d,l,2</sup> , and Michael J. Mitchell<sup>a,m,n,o,p,2</sup> 

Edited by Chad Mirkin, Northwestern University, Evanston, IL; received September 13, 2022; accepted March 29, 2023

Multiple myeloma (MM), a hematologic malignancy that preferentially colonizes the bone marrow, remains incurable with a survival rate of 3 to 6 mo for those with advanced disease despite great efforts to develop effective therapies. Thus, there is an urgent clinical need for innovative and more effective MM therapeutics. Insights suggest that endothelial cells within the bone marrow microenvironment play a critical role. Specifically, cyclophilin A (CyPA), a homing factor secreted by bone marrow endothelial cells (BMECs), is critical to MM homing, progression, survival, and chemotherapeutic resistance. Thus, inhibition of CyPA provides a potential strategy to simultaneously inhibit MM progression and sensitize MM to chemotherapeutics, improving therapeutic response. However, inhibiting factors from the bone marrow endothelium remains challenging due to delivery barriers. Here, we utilize both RNA interference (RNAi) and lipid–polymer nanoparticles to engineer a potential MM therapy, which targets CyPA within blood vessels of the bone marrow. We used combinatorial chemistry and high-throughput in vivo screening methods to engineer a nanoparticle platform for small interfering RNA (siRNA) delivery to bone marrow endothelium. We demonstrate that our strategy inhibits CyPA in BMECs, preventing MM cell extravasation in vitro. Finally, we show that siRNA-based silencing of CyPA in a murine xenograft model of MM, either alone or in combination with the Food and Drug Administration (FDA)-approved MM therapeutic bortezomib, reduces tumor burden and extends survival. This nanoparticle platform may provide a broadly enabling technology to deliver nucleic acid therapeutics to other malignancies that home to bone marrow.

nanomedicine | RNA therapeutics | drug delivery

Multiple myeloma (MM) accounts for ~23% of all hematological malignancies in the United States, with the highest incidences observed in developed countries, including western Europe and Australia (1, 2). Characterized by the accumulation of monoclonal plasma cells in the bone marrow (*SI Appendix, Fig. S1*) (2–4), clinical manifestation of the disease includes anemia causing fatigue, immune paresis leading to infection, renal failure, and osteolytic breakdown of bone by activated osteoclasts, resulting in painful lytic bone destruction (5, 6). Despite recent advances in understanding the pathogenesis of MM, the disease remains incurable, with a 5-y survival rate of ~50% (7). In addition, relapse has become an inevitable part of the disease course, leading to the development of relapsed/refractory MM (RRMM). Patients with RRMM face even shorter survival rates of only 3 to 6 mo (8) and are typically less responsive to standard salvage therapies. Current approaches include using proteasome inhibitors such as bortezomib, a US Food and Drug Administration (FDA)-approved therapy for newly diagnosed and RRMM patients (5). However, following bortezomib therapy, most patients relapse and subsequently develop resistance to such therapy (9, 10). Thus, effective therapeutic strategies are needed to evade resistance in MM.

The inevitability of MM relapse following bortezomib treatment has prompted investigation into the cellular mechanisms that underpin drug resistance. Recent work has demonstrated that the bone marrow microenvironment, and its physical interactions with MM cells, facilitates disease progression and drug resistance (11–14). Through secretome analysis of the bone marrow endothelium, the secreted factor cyclophilin A (CyPA), a ubiquitously abundant protein that is secreted in response to inflammatory stimuli (15, 16), was shown to promote the colonization, proliferation, and drug resistance of MM (17). Thus, the bone marrow microenvironment plays a critical role in disease progression by promoting the adhesion and accumulation of MM cells (17–20). Once secreted by bone marrow endothelial cells (BMECs), CyPA acts as a chemoattractant promoting the migration of MM cells via the CD147 receptor, which leads to the initiation of their proliferation and homing within the bone marrow (Fig. 1*A*) (17). Thus, inhibition of

## Significance

Multiple myeloma (MM) patients face relapse and short survival rates. Thus, there is an urgent clinical need for therapeutic strategies to evade MM drug resistance. Rather than targeting MM directly, the surrounding bone marrow can be targeted to prevent MM homing, proliferation, and drug resistance. Here, we developed a nanoparticle platform to overcome bone marrow delivery barriers and deliver nucleic acid therapeutics. We show that small interfering RNA (siRNA) silencing of a protein secreted by bone marrow, cyclophilin A, inhibits the spread of MM. Additionally, a combination of our platform and FDA-approved MM therapeutic bortezomib dramatically extended mouse survival compared to either treatment alone. This siRNA nanotechnology can potentially serve as a platform to treat other bone marrow-homing malignancies.

This article is a PNAS Direct Submission.

Copyright © 2023 the Author(s). Published by PNAS. This article is distributed under [Creative Commons Attribution-NonCommercial-NoDerivatives License 4.0 \(CC BY-NC-ND\)](https://creativecommons.org/licenses/by-nc-nd/4.0/).

<sup>1</sup>P.P.G.G. and C.G.F.-E. contributed equally to this work.

<sup>2</sup>To whom correspondence may be addressed. Email: Ruben\_Carrasco@dfci.harvard.edu or mjmitch@seas.upenn.edu.

This article contains supporting information online at <https://www.pnas.org/lookup/suppl/doi:10.1073/pnas.2215711120/-/DCSupplemental>.

Published June 13, 2023.

CyPA secretion from BMECs provides a potential therapy to abolish MM cell colonization and proliferation in bone marrow.

To date, there are no small-molecule compounds that effectively inhibit the expression and secretion of CyPA specifically from BMECs. A combination RNA interference (RNAi) approach, which simultaneously inhibits traditionally undruggable targets by directly reducing messenger RNA (mRNA) expression (17), is therefore a promising approach to inhibit MM progression and drug resistance. Small interfering RNA (siRNA) therapeutics have broad potential to reversibly silence any gene and are under development for the treatment of a range of diseases including cancer (18). However, the delivery of siRNA is limited by its instability in the bloodstream and an inability to readily traverse cell membranes; thus, there is a need for safe and effective delivery methods for targeted delivery. Nanoparticle (NP) delivery systems can overcome these obstacles by i) reducing degradation of RNA by endonucleases in blood, ii) avoiding renal clearance,

iii) delivering RNA to specific cells and tissues via functionalization of NP surface chemistry, and iv) mediating target cell entry and cytoplasmic delivery. Of note, the NP-based siRNA therapeutic developed by Alnylam Pharmaceuticals was approved by the FDA in 2018, and the NP-based mRNA vaccines against COVID-19, developed by Moderna and Pfizer/BioNTech, received FDA approval first for emergency use and then for full approval, demonstrating the translatability of NPs for RNA delivery (19–23). Hence, we hypothesized that inhibition of CyPA secretion from BMECs using a siRNA-based therapy using NPs may decrease MM adhesion to BMECs and reduce their ability to colonize the bone marrow.

Here, we developed NPs comprised of a polymer-lipid hybrid material and a lipid-poly(ethylene) glycol (PEG) conjugate to enable nucleic acid encapsulation and in vivo siRNA delivery to the bone marrow. Previously, a polymer-lipid NP design termed 7C1 had been shown to efficiently deliver siRNA to endothelial cells in

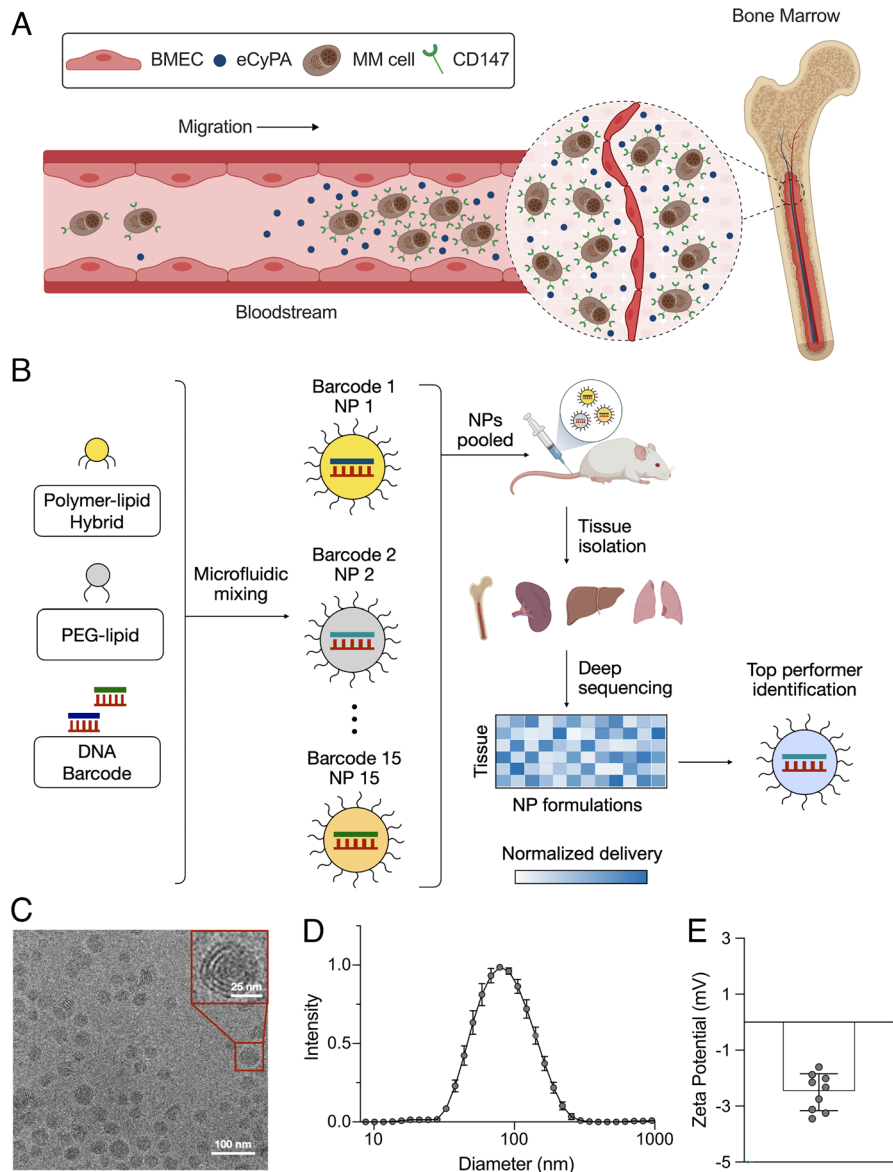


**Fig. 1.** Engineering lipid-polymer nanoparticles (NPs) for siRNA delivery to the bone marrow microenvironment for multiple myeloma therapy. (A) Illustration of CyPA-CD147 complex mediating MM cell migration and bone marrow colonization. Created with BioRender.com. (B) Schematic showing high-throughput in vivo screening to identify NPs for siRNA delivery to bone marrow. A library of 15 NPs encapsulating barcoded DNA was used to determine the top NP formulation for delivery to the bone marrow microenvironment. The lead NP formulation was used to deliver CyPA siRNA to the bone marrow and inhibit MM progression. (C) Cryo-TEM micrograph showing the size and multilamellar structure of the NPs. (D) Hydrodynamic diameter and (E) zeta potential values of the lead (B1) NP formulation. Data are shown as mean  $\pm$  SD.

the lung, heart, and kidney (21). More recently, these formulations were modified to target BMECs to deliver siRNA and sgRNA, and these studies found that the PEG mole percent is a critical factor that influences endothelial cell targeting (22, 23). Similarly, others have shown that small variations in NP composition, such as lipid length or structure, PEG molecular weight, or PEG mole percentage, can drastically impact their biodistribution in the body (24–28). Thus, by altering the lipid length, PEG molecular weight, and PEG mole percentage, we screened 15 unique polymer-lipid NPs simultaneously to determine the lead NP formulation to maximize the delivery of siRNA to BMECs in vivo using a DNA barcoding approach (25, 29).

In the present work, we identified an optimal NP design that delivers siRNA to bone marrow and showed that this formulation successfully silenced CyPA in BMECs. Further, siRNA delivery using our lead NP decreased MM cell adhesion and invasion across BMECs and sensitized MM cells to chemotherapy. Treatment with NPs encapsulating CyPA siRNA (siCyPA) extended survival in a xenograft mouse model of MM, and mouse survival was further extended in combination with the FDA-approved MM drug bortezomib. Together, our results demonstrate how targeting the bone marrow microenvironment, either alone or in combination with therapeutics targeting cancer cells themselves, could be a promising means to treat malignancies like MM that progress following colonization in the bone marrow.

## Results and Discussion

**NP Synthesis and Characterization.** To evaluate NP formulation parameters that enable nucleic acid delivery to the bone marrow microenvironment, we created a library of NP formulations consisting of a polymer–lipid hybrid material and a lipid–polyethylene glycol (PEG) conjugate (21, 22). Low-molecular-weight polyethyleneimine (PEI) and epoxide-terminated lipids were reacted using Michael addition chemistry to synthesize the polymer–lipid hybrid (*SI Appendix, Fig. S2*). NPs were formulated by combining the polymer–lipid, lipid–PEG, and nucleic acids via controlled mixing in a microfluidic device (30). For the barcoding studies, unique DNA barcode strands were encapsulated in each formulation so that they could be detected in each tissue via deep sequencing (Fig. 1*B*). A library of 15 unique NPs was formulated by modifying the following lipid–PEG parameters: i) tail length of the lipid–PEG in the NP membrane (C14, C16, or C18), ii) molecular weight of the PEG surface coating (750, 1,000, 2,000, 3,000, or 5,000 kDa), and iii) PEG surface density on the NP, which was altered by varying the overall molar percentage of PEG within the formulation (20 to 30% by weight) (*SI Appendix, Fig. S2B*).

Cryogenic transmission electron microscopy (cryo-TEM) showed that the resulting NPs have a multilamellar structure and are monodisperse (Fig. 1*C*). Dynamic light scattering measurements showed that each NP formulation was between 80 and 95 nm in diameter (Fig. 1*D* and *SI Appendix, Fig. S2B*). Moreover, zeta potential measurements for each NP in the library ranged from  $-0.6$  to  $-4$  mV (Fig. 1*E* and *SI Appendix, Fig. S2B*), indicating neutral surface charge. We also measured the pKa of a representative NP formulation (B1) to show that the NPs are ionizable (i.e.,  $pK_a < 7.4$ ). To do this, we conducted 6-(p-toluidinyl)naphthalene-2-sulfonate assays, which showed that the B1 NP formulation had a pKa of 7 (*SI Appendix, Fig. S3A*). Further, we complexed this NP with fluorescent siRNA to assess its stability in the bloodstream, and we found that serum fluorescence rapidly decreased within the first 30 min following injection, with a half-life of approximately 12 min (*SI Appendix, Fig. S3B*). Moreover, we confirmed that our B1 NP design remained stable over

3 d in the presence of serum (*SI Appendix, Fig. S3C*). Following characterization, the library of 15 unique NP formulations was used to identify an optimal NP for bone marrow delivery in vivo, as described below.

**NP Barcoding to Target BMECs.** A total of 15 NP formulations encapsulating unique DNA barcodes were pooled together and administered intravenously via tail vein injection into mice. We harvested tissues including the bone marrow, liver, spleen, and lungs and extracted the DNA barcodes 4 h postinjection. The barcodes from each tissue were amplified by PCR and analyzed by deep sequencing to assess the relative biodistribution of each barcode, and therefore, each LNP formulation in various mouse organs. Deep sequencing data identified several NP formulations that preferentially accumulated within the bone marrow, as well as the liver, spleen, and lung (Fig. 2*A–C*). Delivery data was quantified in terms of percent of accumulation of each NP formulation, so that the total NP accumulation within each tissue was 100%. This normalized delivery quantification reflects how efficiently each barcode was delivered to each specific tissue, relative to all other injected barcoded NPs. By quantifying the percent delivery of each NP to the bone marrow, we found that NP formulations B1 and B5 accounted for 22% and 17% of the NPs extracted from bone marrow, respectively (Fig. 2*B*). Interestingly, these two formulations also exhibited high delivery to the spleen and lung as well, relative to the rest of the NP formulations.

To confirm that the percent delivery is indicative of the accumulation of the different NP formulations, and not the barcodes themselves, we prepared several B1 NP formulations that varied in terms of their encapsulated barcodes. We pooled together these NPs such that each barcode comprised different concentrations (0.0001 to 1 mg/kg) of each barcode. NPs were injected into mice intravenously, and the bone marrow, spleen, liver, and lungs were analyzed for barcode delivery. In each of these tissues, delivery was found to be dose dependent (*SI Appendix, Fig. S4*).

Next, we evaluated the ability of these NP formulations to deliver siRNA intravenously to mice to assess whether in vivo silencing of an endothelial cell-specific target gene, Tie2, correlates to barcoded NP delivery in the bone marrow. Following treatment, we conducted RT-qPCR to quantify Tie2 mRNA content in the bone marrow, liver, spleen, and lung. In line with the DNA barcoding delivery results, we found that the B1 NP formulation induced the greatest knockdown of Tie2 mRNA expression compared to the other NP formulations in bone marrow, including the original 7C1 formulation (21) (Fig. 2*C*). Further, plotting percent Tie2 knockdown versus DNA barcode delivery for these NPs showed that although the two parameters were closely correlated in the bone marrow, DNA barcode delivery was not a strong predictor of siRNA knockdown efficiency (23), compared to other tissues such as liver and spleen (Fig. 2*B* and *D*). However, to confirm that functional siRNA delivery observed by the B1 NP formulation was specifically occurring in BMECs, we studied the NP cellular biodistribution, which showed that NPs were primarily taken up by BMECs with a 9.83% uptake, compared to other bone marrow cells such as mesenchymal stromal cells, hematopoietic stem and progenitor cells, and osteoblasts, which each showed an uptake of 2.64%, 0.77%, and 0.44%, respectively (*SI Appendix, Fig. S5A–C*). Further, we evaluated whether we could efficiently silence a protein specifically in BMECs, before further animal studies. For this, we formulated the B1 NP encapsulating siRNA targeting ICAM-2, an endothelial cell surface receptor. We injected ICAM-2 siRNA NPs intravenously, and after 72 h, we measured  $\sim 45\%$  ICAM-2 knockdown in BMECs (*SI Appendix, Fig. S5D* and *E*). These results were in line with previous studies

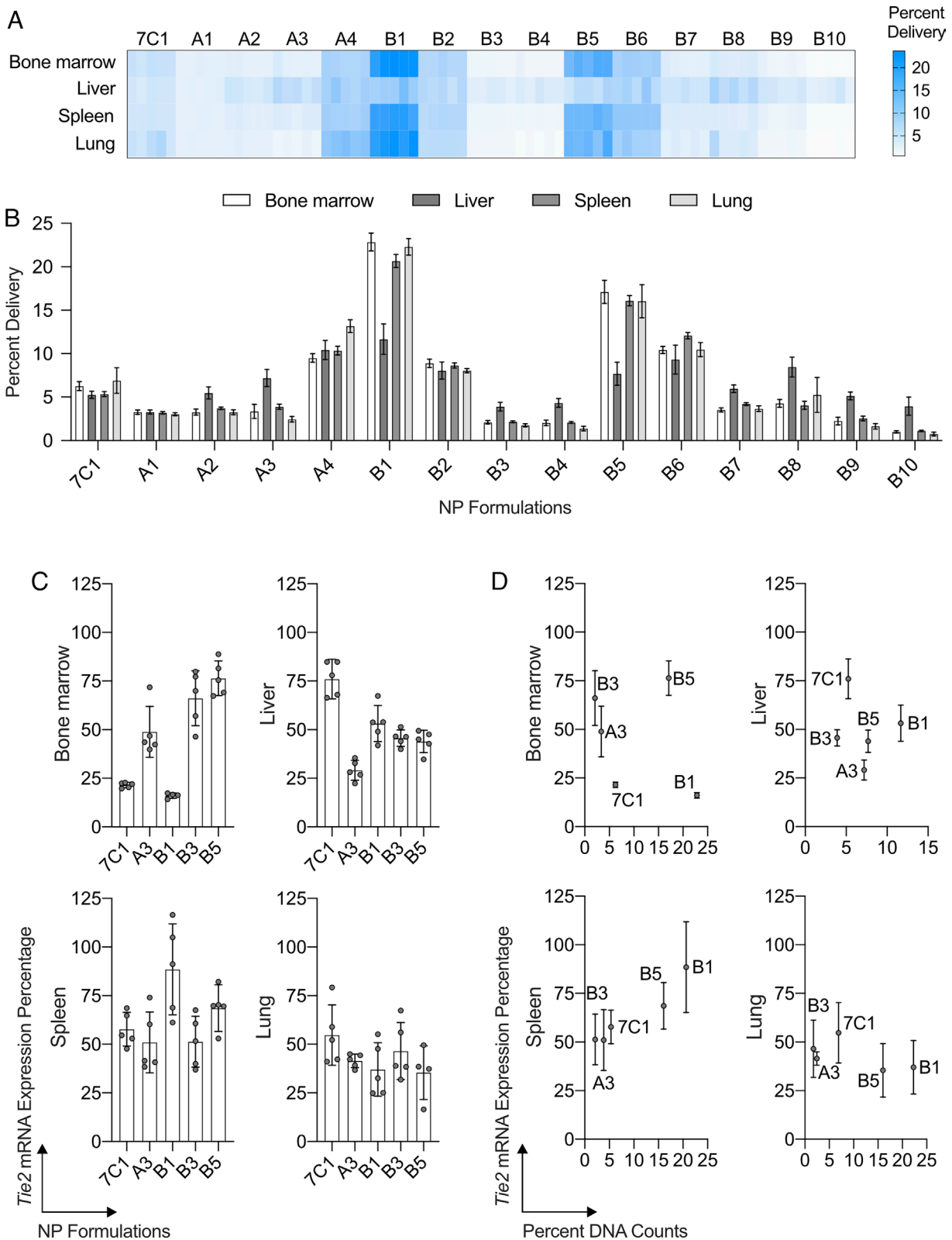


**Fig. 2.** High-throughput DNA nanoparticle barcoding to deliver nucleic acids to bone marrow in vivo. (A) Heat map showing normalized DNA barcode counts in the bone marrow, liver, spleen, and lung measured 4 h following intravenous injection of NPs encapsulating barcoded DNA. Each row represents an individual mouse. (B) Percent delivery of DNA barcodes ( $\pm$ SD) to each tissue. In this quantification, the percent delivery reflects the amount of each barcode delivered as a percentage of total DNA barcode counts in each tissue. (C) Tie2 mRNA expression ( $\pm$ SD) from mice treated with individual NPs encapsulating Tie2 siRNA. Data reflect Tie2 expression 48 h after intravenous injection. (D) DNA barcode delivery ( $\pm$ SD) compared to Tie2 knockdown mediated by NPs encapsulating Tie2 siRNA.  $n = 5$  mice per group.

demonstrating that minimal changes in NP composition, such as PEG molecular weight or PEG mole percentage, largely influence nucleic acid delivery to endothelial cells (22, 23). In addition, we

sought to evaluate whether the top five NP formulations from the in vivo barcoding screen would perform similarly in vitro in BMECs (SI Appendix, Fig. S6A). Interestingly, we found that the B5

formulation outperformed the other four formulations in vitro, which is the opposite to what was seen in vivo for bone marrow (Fig. 2C). This phenomenon has been observed previously, where in vivo and in vitro screening methods have shown little to no

correlation (31). However, the other four formulations showed similar gene silencing abilities (*SI Appendix, Fig. S6 B and C*). Altogether, we identified a unique NP formulation (B1) with potent silencing in BMECs in vivo and in vitro.

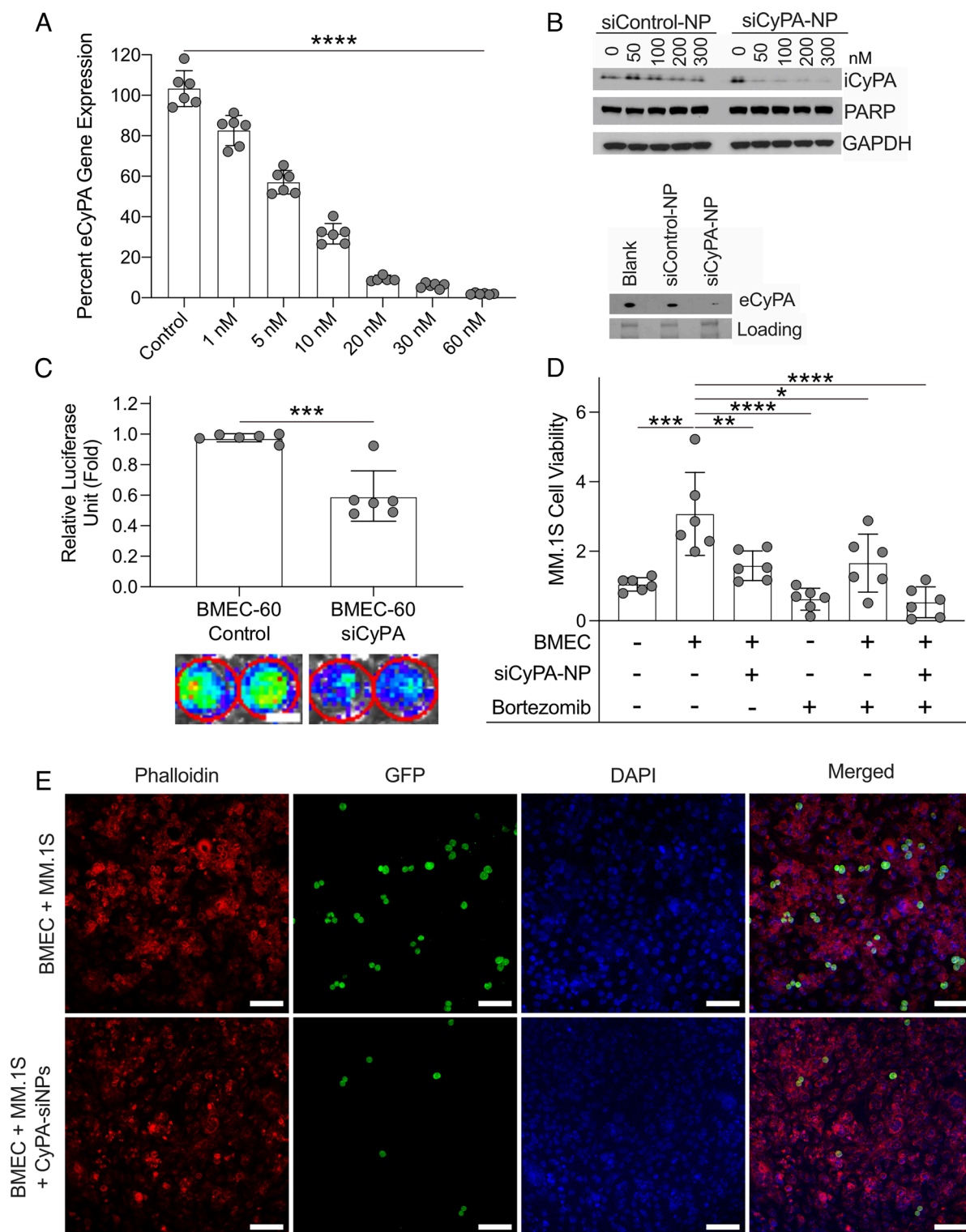


**Fig. 3.** Nanoparticle-based siRNA silencing of CyPA abolishes physical interactions between bone marrow endothelium and tumor cells. (A) Extracellular CyPA expression ( $\pm$ SD) by murine endothelial cells (bEnd.3) treated with 1 to 60 nM siCyPA-NPs for 24 h prior to RT-qPCR analysis ( $n = 6$ ,  $P < 0.0001$ ; one-way ANOVA with multiple comparisons). (B) Western blot showing intracellular and extracellular CyPA expression in BMECs following treatment with 0 to 300 nM siCyPA-NPs or siControl-NPs. (C) Luc+ MM.1S cell invasion ( $\pm$ SD) through monolayers of BMECs treated with siControl-NPs or siCyPA-NPs ( $n = 6$ ,  $P < 0.001$ , unpaired two-tailed  $t$  test). (Scale bars, 10  $\mu$ m.) (D) Cell viability ( $\pm$ SD) of MM cells alone or in coculture with BMECs and treated with 1 nM bortezomib with or without 60 nM siCyPA-NPs ( $n = 6$ ,  $*P < 0.05$ ,  $**P < 0.01$ ,  $***P < 0.001$ ,  $****P < 0.0001$ ; one-way ANOVA with multiple comparisons). (E) Representative images showing MM cell adhesion to BMEC monolayers treated with 60 nM siCyPA-NPs. (Scale bars, 100  $\mu$ m.)

**Silencing CyPA Decreases MM Cell Invasion across BMEC Monolayers.** After determining the top formulation for delivering nucleic acids to bone marrow *in vivo*, we next evaluated how B1 NPs deliver siCyPA *in vitro* to BMECs and its subsequent effects on MM cell invasion. As previously stated, CyPA is a ubiquitously abundant protein, that is secreted as a response to inflammatory stimuli (15), and was shown to be expressed much lower in endothelial cells from other tissues than those in the bone marrow in the context of MM, having a critical role in promoting the homing and colonization of MM cells within the bone marrow microenvironment (17). Therefore, we chose to deliver siCyPA to BMECs to inhibit MM cell invasion into the bone marrow and halt disease progression. First, we screened a library of 12 mouse or human siCyPA sequences to determine the best sequences for silencing CyPA (SI Appendix, Figs. S7 and S8). The top mouse or human siRNA sequences were encapsulated within B1 NPs (siCyPA-NPs) and were evaluated *in vitro* for their silencing abilities. We then treated murine endothelial cells (bEnd.3 cells) with siCyPA-NPs at concentrations ranging from 1 to 60 nM of siCyPA. After 24 h treatment, we evaluated CyPA expression using RT-qPCR, which showed a dose-dependent decrease in CyPA expression (Fig. 3A).

To examine the potential of silencing CyPA in human MM disease, we replaced the siRNA in siCyPA-NPs with the top human siRNA sequence. We treated human BMECs with siCyPA-NPs

for 24 h and quantified intracellular or secreted CyPA content by western blotting. BMECs treated with siCyPA-NPs exhibited decreased intracellular and extracellular CyPA expression following treatment compared to both empty NPs and control NPs that were complexed with control siRNA (siControl-NPs), without induction of BMEC cell death (Fig. 3B). Next, we conducted transwell assays to assess how CyPA silencing impacts the ability of MM cells to invade across BMEC monolayers. BMECs were treated with siCyPA-NPs or siControl-NPs, followed by coincubation with Luc+/GFP+ MM cells. After 24 h, we imaged and quantified the luminescent signal from the MM cells that invaded through BMEC monolayers, which revealed 40% lower luciferase signal when BMECs were treated with siCyPA-NPs compared to siControl-NPs (Fig. 3C). This indicates that CyPA silencing in BMECs inhibits the ability of MM cells to invade across BMEC monolayers, which we anticipate would inhibit MM homing to the bone marrow and invasion across BMECs *in vivo*. Collectively, these data demonstrate that siCyPA-NPs induce potent gene silencing in BMECs and significantly reduce MM cell invasion, without cytotoxic effects.

**Treating BMECs with siCyPA-NPs Sensitizes Cells to Bortezomib Therapy *In Vitro*.** As previously discussed, the homing and colonization of MM cells in the bone marrow potentially decreases the sensitivity of these cells to standard therapies. Thus,

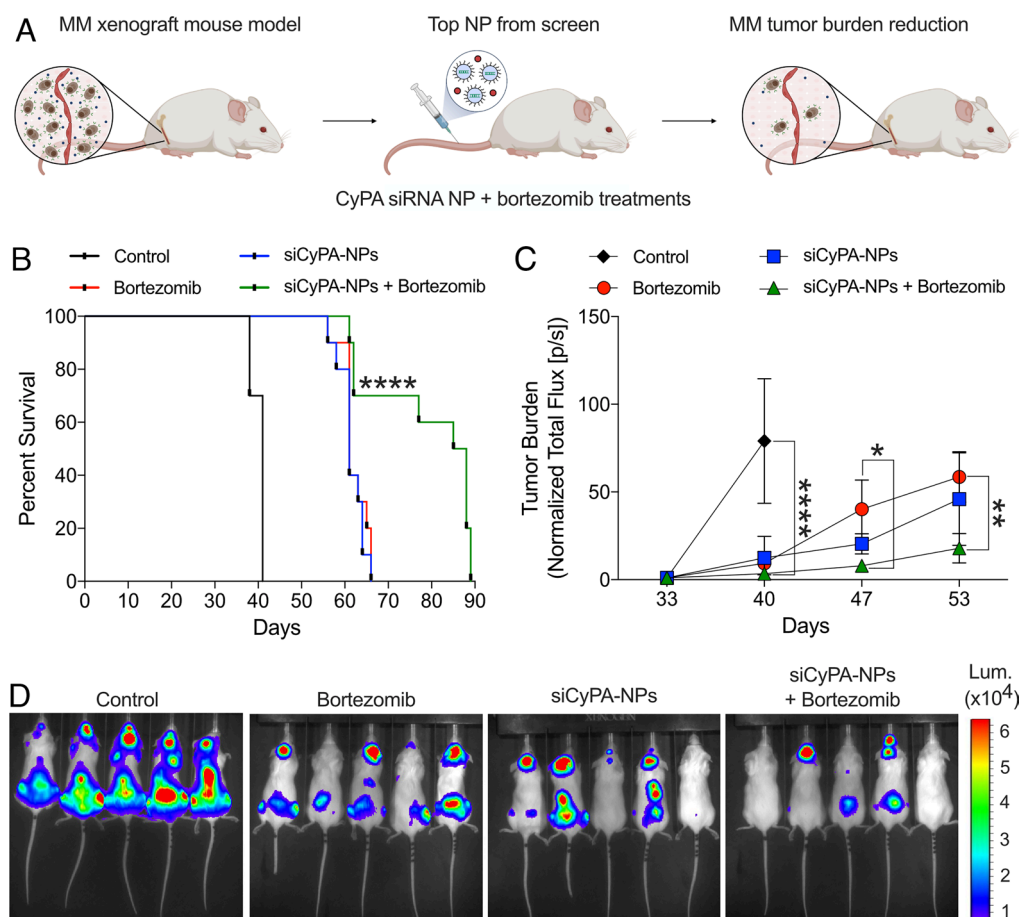


**Fig. 4.** Combination of siCyPA-NPs and bortezomib synergistically improves overall survival and reduces tumor burden in a MM mouse xenograft model. (A) Overview of NP-based siRNA and bortezomib combination therapeutic strategy to treat MM. (B) Kaplan-Meier survival curves of mice with MM tumors following treatment with PBS, bortezomib, siCyPA-NPs, or a combination of bortezomib and siCyPA-NPs ( $n = 10$  mice per group, \*\*\*\* $P < 0.0001$  with log-rank test). (C) Tumor burden as quantified by normalized total flux ( $\pm$ SD) from bioluminescence imaging ( $n = 5$  mice per group each, \* $P < 0.05$ , \*\* $P < 0.01$ , \*\*\*\* $P < 0.0001$ ; two-way ANOVA with mixed-effects analysis). (D) Representative bioluminescence images of mice at day 40. The scale represents luminescence signal from Luc+ MM.1S cells, which was used to quantify tumor burden in part (B). Mice in this study were injected intravenously with Luc+ MM.1S cells on day 0. Treatments were injected intravenously or intraperitoneally twice a week starting on day 30.

we anticipated that decreasing MM cell adhesion to BMECs by silencing CyPA could sensitize these cells to treatment with the FDA-approved proteasome inhibitor bortezomib, which is used in the clinic to treat MM (2).

MM and BMECs either alone or in coculture were treated with bortezomib at 1 nM and siCyPA-NPs at 60 nM either individually or in combination, and cell viability was assessed after 24 h (Fig. 3D). Treatment of MM cells with bortezomib decreased the viability of MM cells more than 1.5-fold compared to untreated cells. Coculturing MM cells with BMECs resulted in a significant increase in viability compared to coculturing MM cells with siCyPA-NP-treated BMECs, demonstrating that the secretion of CyPA from BMECs promotes the proliferation of MM. This also suggests that the interactions between MM cells and BMECs make MM cells more resistant to bortezomib treatment (Fig. 3D) (9).

However, treatment of BMECs with siCyPA-NPs prior to the addition of MM cells and bortezomib to the coculture resensitized MM cells to bortezomib (10), as evidenced by the 2.5-fold reduction in viability compared to no siCyPA-NP treatment (Fig. 3D).

**Treating BMECs with siCyPA-NPs Disrupts Interactions with MM Cells In Vitro.** To confirm that CyPA silencing reduced adhesion of MM cells to BMECs, we cultured MM cells on BMEC monolayers and evaluated their ability to adhere to BMECs. Treating BMECs with siCyPA-NPs prior to the addition of GFP+ MM.1S cells decreased their ability to adhere to BMECs, as evidenced by the reduced number of GFP-expressing cells (Fig. 3E). Together, the results from the in vitro experiments described here indicate that siCyPA-NPs can inhibit the ability of MM cells to adhere and invade through BMEC monolayers, thus sensitizing these cells to

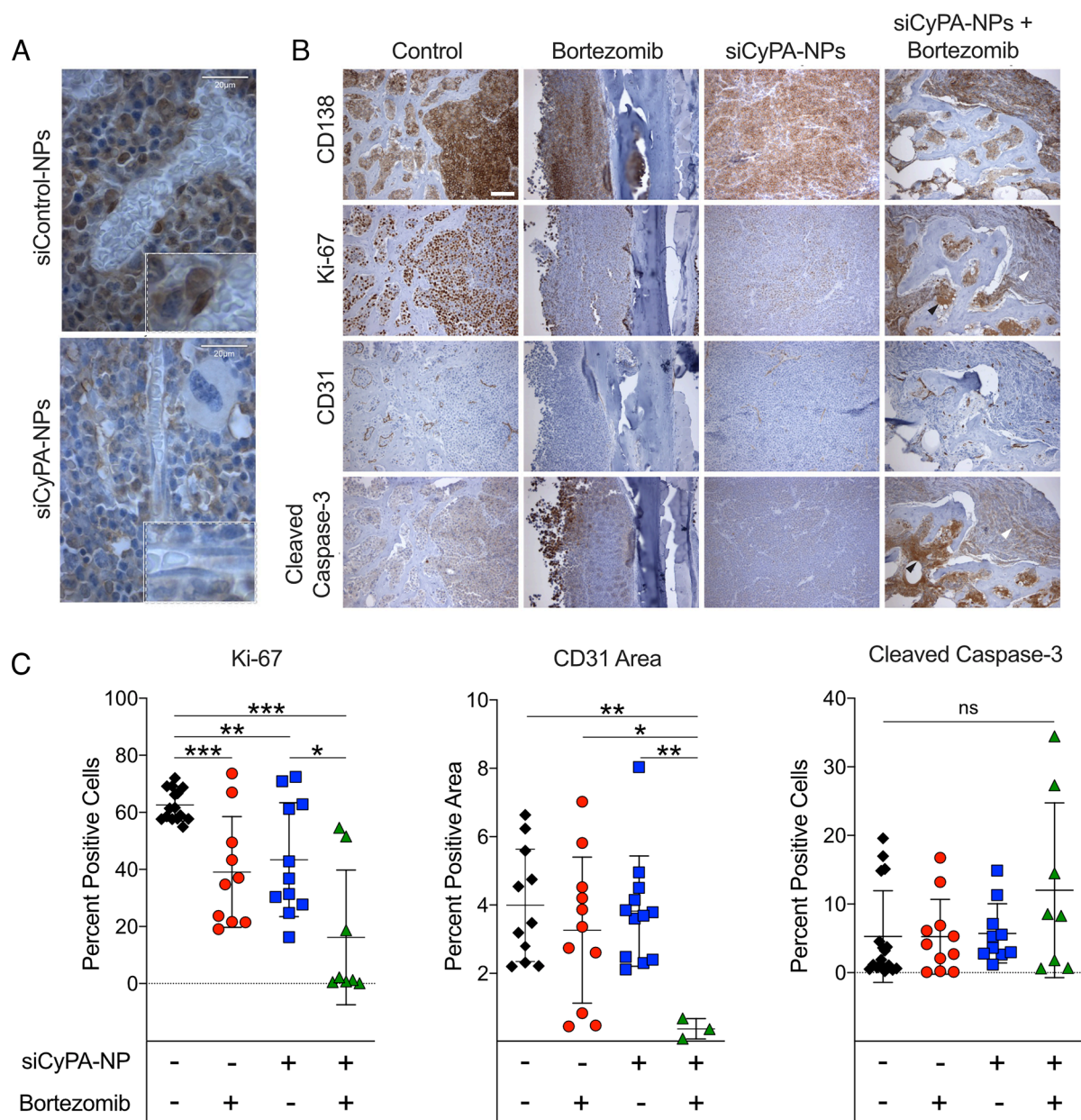


**Fig. 5.** Cotreatment of siCyPA-NPs and bortezomib decreases tumor cell proliferation and angiogenesis. (A) Representative immunostaining for CyPA expression in the bone marrow of mice treated with siControl-NPs or siCyPA-NPs. Red/brown stain is positive for CyPA. (Scale bars, 20  $\mu$ m.) (B) Representative immunostaining and (C) quantifications for CD138, Ki-67, CD31, and cleaved caspase-3 ( $\pm$ SD) in sections of bone marrow following treatment with PBS, bortezomib, siCyPA-NPs, or both bortezomib and siCyPA-NPs. Red/brown stain is positive for each protein marker. Arrowheads indicate significant change in staining. (Scale bars, 100  $\mu$ m) (n = at least 3 mice per group, \* $P$  < 0.05, \*\* $P$  < 0.01, \*\*\* $P$  < 0.001; one-way ANOVA with multiple comparisons).

bortezomib treatment. Collectively, these results set the rationale to evaluate this combination therapy in vivo.

### Cotreatment with siCyPA-NPs and Bortezomib Decreases Tumor Burden and Extends Survival in a Mouse Xenograft Model of MM.

To assess the therapeutic potential of siCyPA-NPs in vivo, we first injected  $2 \times 10^6$  Luc+/GFP+ MM.1S cells via tail vein injection and allowed tumors to grow for 30 d prior to NP or bortezomib treatment (Fig. 4A). On day 30, mice were intravenously injected with 1 mg/kg siCyPA-NPs or siControl-NPs with or without 0.5 mg/kg bortezomib. Subsequently, the mice were injected twice a week via intravenous injection of NPs or intraperitoneally (i.p.) with bortezomib. The mice were imaged once a week using an in vivo imaging system (IVIS), and tumor burden was quantified as a total flux output. All treatment groups substantially reduced tumor burden compared to mice treated with only phosphate-buffered saline (PBS) solution. However, treating mice with both siCyPA-NPs and bortezomib caused the greatest inhibition of tumor burden compared to each therapy administered alone (Fig. 4B and C). These results corresponded to extended mouse survival up to 90 d, compared to 65 d for mice treated with siCyPA-NPs or bortezomib only (Fig. 4B). Importantly, mice treated with bortezomib and siControl-NPs exhibited similar survival compared to bortezomib alone, indicating that siCyPA-NPs were essential to sensitize MM cells to bortezomib treatment in vivo. Together, these results indicate that targeting CyPA secretion via siCyPA-NPs disrupts MM progression in mice in vivo and extends survival in a mouse model of MM.

**siCyPA-NPs and Bortezomib Therapy Decrease MM Cell Proliferation and Angiogenesis.** To assess whether siCyPA NPs and bortezomib decreased MM cell proliferation and angiogenesis, bone marrow from treated mice was collected and analyzed for cell surface markers by histology to understand the mechanisms behind this therapy. First, we assessed CyPA knockdown in BMECs in the bone marrow following treatment with siCyPA-NPs. Immunostaining showed that bone marrow myeloid cells exhibited high levels of CyPA expression, and the expression was significantly lower for mice treated with siCyPA-NPs, which confirmed knockdown of CyPA following treatment (Fig. 5A). Staining for CD138 was used to stain plasma cells and to indicate where tumor tissue was located within the bone marrow (Fig. 5B). We imaged and quantified the percentage of positive cells for proliferation and apoptosis (Ki-67 and cleaved caspase 3, respectively) or percent positive area for angiogenesis (CD31) (Fig. 5B and C). Cleaved caspase 3 staining revealed only a modest increase in apoptotic cells in tumor areas (Fig. 5B and C). However, there were significant decreases in both proliferation and angiogenesis within tumor regions following treatment with siCyPA-NPs compared to the individual treatments (Fig. 5C). Quantification of proliferation and angiogenesis within tumor regions revealed that treatment with siCyPA-NPs decreased each fourfold and threefold, respectively, as indicated by the white and black arrowheads in Fig. 3B. These results suggest that the increased survival in mice following siCyPA-NP and bortezomib therapy could be due to decreased cell proliferation and reduced formation of blood vessels, suggesting that these tumors are underdeveloped tumors compared to the control experimental group.

Overall, this work shows that the siCyPA-NP system has the potential to be an effective MM therapy, particularly in combination with bortezomib treatment. The silencing of CyPA decreased MM invasion across BMECs and disrupted interactions between BMECs and MM cells. When combined with bortezomib, CyPA silencing sensitized MM cells to therapy, which reduced proliferation and

angiogenesis, and ultimately extended mouse survival. Furthermore, our in vivo screening results concur with those of previous reports using PEI for NP-based drug delivery, specifically for endothelial cell targeting (21, 23, 25), and further confirmed that NP composition is critical to enhance tissue specificity (22, 24, 25, 27). In addition, we also showed a weak correlation between in vivo and in vitro screening results, where the NP least effective in vivo outperformed the rest of the NP formulations in vitro, which is in line with what others have previously published in the field (31). To conclude, we believe that beyond MM therapeutics, the presented system could be modified for siRNA delivery to other inflammatory sites, whether for CyPA or other relevant therapeutic targets in a variety of diseases. For example, we show siRNA delivery to the lung (Fig. 2C), where CyPA has been shown to have a crucial role in pulmonary arterial hypertension and non-small cell lung cancer (32–34). Thus, we consider that this study demonstrates the potential to develop NPs to target other vascular beds in vivo and the advancement in the field for RNAi-based therapeutics. Using nucleic acid therapeutics, this platform could control the interactions between a range of endothelial cell and cancer cell types. Broadly, this study presents a combinatorial therapeutic strategy to target the bone marrow microenvironment, rather than cancer cells themselves, as means to treat MM, which could be extended to treat other blood malignancies, or malignancies that metastasize to bone.

## Materials and Methods

**Polymer-Lipid Synthesis.** Polymer-lipids were synthesized by reacting low-molecular-weight PEI (Sigma-Aldrich, St. Louis, MO, USA) with C15 epoxide-terminated alkyl tails (Tokyo Chemical Industry, Tokyo, Japan) at 90 °C in 100% ethanol for 48 to 72 h at a 14:1 molar ratio as described previously (21, 30). Polymer-lipids were purified via flash chromatography to separate the optimized hydrophobic C15:hydrophilic PEI ratio, as described previously (21).

**Polymer-Lipid NP Formulation.** NPs were formed by combining an aqueous phase containing siRNA with an ethanol phase comprised of polymer-lipids and a polyethylene glycol (PEG)-lipid conjugate via controlled mixing in a microfluidic device (29, 35). Specifically, the ethanol phase contained the polymer-lipid and a PEG-lipid conjugate that varied in terms of the length of the lipid (C14, C16, or C18), PEG molecular weight (750, 1,000, 2,000, 3,000, or 5,000 kDa), or PEG mole percentages (20 or 30% by weight) (Avanti Polar Lipids, Alabaster, AL, USA) as shown in Fig. 1. The aqueous phase was prepared in 10 mM citrate, pH 3.0 buffer (Teknova, Hollister, CA, USA) with barcoded DNA (b-DNA) or siCyPA. Syringe pumps were used to perfuse the ethanol and aqueous phases at a 2.5:1 ratio through the microfluidic device (29). The resulting NPs were dialyzed against PBS at room temperature for 3 h and then extruded through a 0.22- $\mu$ m sterile filter (Genesee Scientific, San Diego, CA, USA) (29). For the b-DNA experiments, unique DNA barcode strands were complexed into each formulation so that they could be detected in each tissue via deep sequencing (Fig. 1B).

**NP Characterization.** DNA or siRNA concentration in NPs for in vitro and in vivo use was quantified using a NanoDrop Spectrophotometer (Thermo Fisher Scientific, Waltham, MA, USA) and a modified Quant-iT RiboGreen RNA assay (Thermo Fisher Scientific) as previously described (29, 36). NP hydrodynamic diameter, polydispersity (PDI), and surface charge were measured using a Zetasizer Nano ZS machine (Malvern Panalytical, Malvern, UK). For analysis of NP structure using cryo-TEM, NP samples were prepared in a vitrification system (25 °C, ~100% humidity). Briefly, 3  $\mu$ L sample of NP solution was dropped on a lacey copper grid coated with a continuous carbon film and blotted to remove excess sample without damaging the carbon layer. A grid was mounted on a Gatan 626 single tilt cryogenic holder equipped in the TEM column. Images of NP samples were recorded on an UltraScan 1000 CCD camera (Gatan, Pleasanton, CA). For stability studies, the hydrodynamic diameter of the top-performing NP design was measured over 3 d, in a PBS solution supplemented with 10% of mouse serum, to mimic the in vivo environment (SI Appendix, Fig. S3C).



**b-DNA Design.** b-DNAs were single-stranded DNAs that consisted of 61 nucleotides with 5 consecutive phosphorothioate bonds at each end. The barcode region was composed of 10 nucleotides in the center of the oligonucleotide. An additional 10 random nucleotides were included at 3' end of the barcode region. The 5' and 3' ends of each b-DNA were conserved and contained priming sites for Illumina adapters. A full list of b-DNA sequences can be found in *SI Appendix, Table S1*. All oligonucleotides in this study were synthesized and purified (standard desalting procedure) by Integrated DNA Technologies (Coralville, IA, USA).

**In Vivo Barcoded NP Delivery.** To evaluate b-DNA delivery, each b-DNA containing a different barcode sequence was encapsulated in different NPs from the library and intravenously administered at various concentrations (0.0001 to 1 mg/kg) in 6 to 8-wk-old female C57BL/6 mice, purchased from Charles River Labs (Wilmington, MA, USA), as a single pool ( $n = 5$ ) (Fig. 1*B*). For all experiments, tissues were harvested 4 h postinjection. The tissues were snap-frozen in liquid nitrogen, disrupted into powder using a Geno/Grinder (SPEX SamplePrep, Metuchen, NJ, USA), and stored in a  $-80^{\circ}\text{C}$  freezer. To quantify b-DNA delivery in vivo, b-DNA from different tissues was isolated to obtain barcode counts via deep sequencing.

**Deep Sequencing and Barcode Sequencing Normalization.** All deep-sequencing runs were performed using multiplexed runs on an Illumina MiSeq (Illumina, Metuchen, NJ, USA). PCR product pools were quantified using the KAPA Library Quantification Kit for next-generation sequencing. PCR product pools were loaded onto flow cells at 4 nM concentration. Python scripts were written to quantify barcodes from Illumina fastq files. Normalized b-DNA delivery of a specific barcode to a certain tissue was calculated by dividing the number of sequencing reads of one barcode delivered by a single NP formulation by the total amount of reads from all barcodes delivered by all NPs in a specific tissue.

**Tie2 Gene Silencing.** To validate the b-DNA NP screening results, using Tie2 siRNA, C57BL/6 mice (Charles River Labs, Wilmington, MA, USA) were treated with a single dosage of Tie2 siRNA NPs (1.0 mg/kg), and femurs were harvested 48 h postinjection. The mice were killed by  $\text{CO}_2$  asphyxiation, and the femurs were harvested and immediately snap-frozen in liquid nitrogen. The frozen tissues were pulverized to form a powder using a SPEX 2010 Geno/Grinder (SPEX SamplePrep, Metuchen, NJ, USA). Tissue lysates were prepared in Tissue and Cell Lysis Buffer supplemented with 0.5 mg/mL Proteinase K (Epicentre, Madison, WI, USA). Tissue samples were mixed at 1,400 revolutions per minute (RPM) for 2 h at  $65^{\circ}\text{C}$  and then centrifuged at 11,000 RPM to remove bone debris. mRNA levels in the supernatant were quantified using the QuantiGene 2.0 luminescent-based branched DNA (bDNA) assay kit and the QuantiGene 2.0 probes against Tie2 and GAPDH (Thermo Fisher Scientific, Waltham, MA, USA) according to the manufacturer's protocol. Luminescent signals were measured using a Tecan Infinite 200 PRO plate reader (Tecan, Männedorf, CH). Standard curves for femur tissues and each target gene were constructed using samples from untreated mice, to ensure optimal dilutions for assay samples that avoid luminescent signal saturation. Tie2 silencing in treated mice was quantified by calculating the ratio of Tie2 gene luminescence to GAPDH gene luminescence, with all values normalized to Tie2:GAPDH gene ratios from untreated mice. For in vitro Tie2 silencing, BMEC-60 cells were plated in 24-well plates (150,000 cells per well) and incubated for 24 h prior to treatment with Tie2 siRNA NPs (7C1, A3, B1, B3, and B5) at a dose of 5 or 50 nM or their counterpart control siRNA NP at the same doses. Samples were then incubated for 24 h prior to gene expression analysis. Briefly, the cells were washed with PBS and harvested using 0.25% of trypsin. The cells were disrupted using the Monarch<sup>®</sup> Total RNA Miniprep Kit (New England BioLabs<sup>®</sup>, Ipswich, MA, USA), and RNA was stored in a  $-20^{\circ}\text{C}$  freezer until further use. Luna<sup>®</sup> Universal One-Step RT-qPCR Kit (New England BioLabs<sup>®</sup>) was used to obtain Tie2 mRNA expression for the different NP treatments. Data analysis, as mentioned above, was carried out using GAPDH as the housekeeping gene.

**Flow Cytometry.** Single-cell suspensions were obtained from bone marrow. Briefly, mice were killed, and legs were collected from each mouse in each respective group. Bone marrow cells (*SI Appendix, Fig. S5A*) were collected by flushing femurs in PBS with 0.5% bovine serum albumin. Cells were then plunged through a 70- $\mu\text{m}$  nylon mesh (BD, Franklin Lakes, NJ, USA), washed, and centrifuged (8 min, 300g,  $4^{\circ}\text{C}$ ). The obtained single-cell suspensions were stained at  $4^{\circ}\text{C}$

for 30 min and afterward washed, centrifuged, and resuspended. We used the following fluorochrome-conjugated antibodies (BioLegend, San Diego, CA, USA) specific to mouse: Ter119 (clone TER119), Sca-1 (clone D7), CD31 (clone 390), CD45 (clone 13/2.3), CD51 (clone RMV-7), c-kit (clone ACK2), Lineage (clones 145-2C11, RB6-8C5, RA3-6B2, TER119, M1/70), and CD102 (ICAM-2, clone 3C4). Endothelial cells were gated as CD45<sup>+</sup> Ter119<sup>+</sup> CD31<sup>+</sup> Sca-1<sup>+</sup> (22). Osteoblasts were gated as CD45<sup>+</sup> Ter119<sup>+</sup> CD31<sup>+</sup> CD51<sup>+</sup> Sca-1<sup>+</sup> and mesenchymal stromal cells as CD45<sup>+</sup> Ter119<sup>+</sup> CD31<sup>+</sup> CD51<sup>+</sup> Sca-1<sup>+</sup> (37). Hematopoietic stem and progenitor cells were gated as Lineage<sup>+</sup> c-kit<sup>+</sup> Sca-1<sup>+</sup> (22). To determine NP uptake in different cell types, B1 NP was labeled with DiOC<sub>18</sub> (7) (DiR; Thermo Fisher Scientific, Waltham, MA, USA). Using cells from noninjected mice as a negative control, the positivity for DiR-NP uptake was determined (*SI Appendix, Fig. S5*). Data were acquired on an LSRII system (BD) and analyzed with FlowJo software (BD).

**Cell Culture.** The human bone marrow-derived endothelial cell line BMEC-60 (38) was cultured in EBM-2 Basal Medium containing supplements and growth factors required (Lonza, Morristown, NJ, USA). The mouse endothelial cell line bEnd.3 (ATCC no. CRL-2299) was cultured in Dulbecco's Modified Eagle Medium (Thermo Fisher Scientific, Waltham, MA, USA) supplemented with 10% of fetal bovine serum (FBS). MM.1S (ATCC no. CRL-2974) cells were cultured in Roswell Park Memorial Institute 1640 medium (Thermo Fisher Scientific) supplemented with 10% FBS. All cell lines were grown at  $37^{\circ}\text{C}$  under a 5%  $\text{CO}_2$  humidified atmosphere until confluence.

**CyPA Knockdown.** To investigate CyPA knockdown efficiency, bEnd.3 cells were plated in 24-well plates (150,000 cells per well) and incubated for 24 h prior to treatment with siCyPA-NPs or siControl-NPs. A serial dilution of each siRNA NP formulation in PBS was prepared at concentrations of 1 to 60 nM siRNA. Samples were then incubated for 24 h prior to gene expression analysis. Cells were washed with PBS and harvested using 0.25% trypsin. The cells were disrupted and resuspended in TRIzol<sup>™</sup> (Thermo Fisher Scientific, Waltham, MA, USA), and RNA was extracted following the manufacturer's protocol. Briefly, 2  $\mu\text{g}$  of RNA was DNase treated using a 10- $\mu\text{L}$  reaction containing 1 U/ $\mu\text{L}$  RQ1 DNase, 1X RQ1 DNase buffer, and 20 U/ $\mu\text{L}$  RNAse inhibitor for 30 min at  $37^{\circ}\text{C}$  and stopped with the addition of 1  $\mu\text{L}$  STOP solution followed by a 10-min incubation at  $65^{\circ}\text{C}$ . One microliter Oligo dT was added to each reaction and denatured for 5 min at  $70^{\circ}\text{C}$  and moved immediately to ice. Reverse transcription of the DNase-treated RNA was carried out in a 20- $\mu\text{L}$  reaction using 1  $\mu\text{L}$  GoScript Reverse Transcriptase (Promega, Madison, WI, USA) containing a final concentration of  $1\times$  GoScript Reaction Buffer, 2.5 mM  $\text{MgCl}_2$ , 0.5 mM dNTPs using the following cycling:  $25^{\circ}\text{C}$  for 5 min,  $42^{\circ}\text{C}$  for 1 h,  $70^{\circ}\text{C}$  for 15 min,  $4^{\circ}\text{C}$  hold.

**Immunoblot Analysis.** Total protein samples were prepared from nonattached MM.1S cells grown for 72 h in the presence of BMEC-60 (Luc+/GFP+ MM.1S, Luc+/GFP+ MM.1S-siControl-NPs or Luc+/GFP+ MM.1S-siCyPA-NPs). MM.1S cells were cultured with BMEC-60 cells using 0.45- $\mu\text{m}$  pore diameter transwell chambers (Corning-Costar, Cambridge, MA, USA). Immunoblotting was performed as described (17). For the treatment of MM.1S cells, the cells were incubated with siControl-NPs or siCyPA-NPs for 72 h in 0.5% FBS (Gibco, Amarillo, TX, USA) supplemented medium, followed by protein preparation. Human primary antibodies CyPA (Abcam, Cambridge, UK) and PARP (Cell Signaling Technology, Danvers, MA, USA) were used, and actin was used as a loading control. Secondary antibodies included anti-rabbit IgG horseradish peroxidase (HRP)-conjugated (Promega, Madison, WI, USA) and anti-mouse IgG HRP-conjugated (Promega). Intracellular and extracellular CyPA protein expression following treatment with 0 to 300 nM siCyPA-NPs or siControl-NPs was measured in triplicate by Bradford assay (Bio-Rad, Hercules, CA, USA). Optimal antibody concentrations were used according to the manufacturer's recommendations.

**Transmigration Assays.** To perform the cell migration assay, the top chamber of a transwell plate (8- $\mu\text{m}$  pore diameter, Corning-Costar, Cambridge, MA, USA) was seeded with  $2 \times 10^5$  cells (Luc+/GFP+ MM.1S, Luc+/GFP+ MM.1S-siControl-NPs or Luc+/GFP+ MM.1S-siCyPA-NPs), and the bottom chamber was seeded with medium alone (RPMI with 0.1% FBS) or in the presence of cells (BMEC-60, BMEC-60-siControl NPs or Luc+/GFP+ MM.1S-siCyPA-NPs). After 12 h of incubation, Luc+/GFP+ MM.1S cells that had migrated to the bottom chamber were collected

and quantified using an IVIS imaging system (Caliper Life Sciences, Waltham, MA, USA). Migration data were normalized using data obtained with medium alone. The results are mean  $\pm$  SD for triplicate assays.

**Cell Adhesion and Viability Assays.** To investigate cell adhesion and cell viability, BMEC-60 cells were plated in 8-well chambers (ibidi GmbH, Munich, Germany) or 96-well plates (15,000 cells/mL per well) and incubated for 48 to 72 h prior to addition of MM.1S cells (35,000 cells/mL per well) followed by treatment with PBS, siCyPA-NPs (60 nM), or bortezomib (1 nM), or siCyPA-NPs (60 nM) and bortezomib (1 nM). Monolayers were stained with cell mask (red) and DAPI (blue) for easier GFP+ MM.1S identification and fixed with 4% (wt/vol) paraformaldehyde (PFA) prior to imaging. The adhesion and viability of Luc+/GFP+ MM.1S cells was determined after coculture with BMEC-60 cells and treatment as described above, using confocal microscopy, a CellTiter-Glo Luminescent Cell Viability Assay, and in vitro bioluminescence imaging (BLI).

**Animal Studies.** All animal procedures conducted at the University of Pennsylvania were approved by the Institutional Animal Care and Use Committees and were in accordance with local, state, and federal regulations. For the in vivo efficacy studies, severe combined immunodeficient female mice with a non-obese diabetic background (Nod/SCID) were injected via tail vein with Luc+/GFP+ MM.1S cells and randomly divided into four groups after 30 d (n = 10). After injecting MM.1S cells, on day 30, mice were treated with the following: i) PBS, ii) free drug (bortezomib), iii) siControl-NPs, iv) siCyPA-NPs, and v) siCyPA-NPs and bortezomib. The mice were injected i.p. twice a week with 0.5 mg/kg bortezomib or via intravenous injection of scrambled-NPs or siCyPA-NPs (1 mg/kg). The mice were imaged once a week via BLI to assess tumor burden. Briefly, the mice were injected with 100  $\mu$ L luciferin (Caliper Life Sciences, Waltham, MA, USA) at 30 mg/mL, followed by whole-body real-time BLI using an IVIS (Caliper Life Sciences) 10 min after injection. Total flux (photons per second) was quantified as the sum of all detected photon counts within a region of interest of 4  $\times$  8-cm for the whole body. The mice were killed via CO<sub>2</sub> inhalation at end points described or, for survival studies, when they had hindlimb paralysis, had cachexia, had weight loss of >15%, or become moribund. Survival data of mice with MM.1S tumors following treatment were assessed.

**Histopathological and Immunohistochemical Analyses.** Tissue sections were processed as previously described (39). The sections were incubated with primary antibodies (5  $\mu$ g/mL) or the corresponding IgG fraction of preimmune serum overnight at 4 °C in blocking solution (3% BSA in PBS). Antihuman primary specific antibodies included: CD138 (Beckman Coulter, Chaska, MN, USA), CD31 (Abcam, Cambridge, UK), caspase-3 (Cell Signaling Technology, Danvers, MA, USA), CyPA (Abcam), and Ki-67 (Abcam) and were visualized with the aid of the corresponding biotinylated antibody coupled to streptavidin-peroxidase complex (Vector Labs, Burlingame, CA, USA). For negative controls, tissue sections were incubated in the absence of primary antibodies or preimmune serum from the species of origin of the primary antibody. Optimal antibody concentrations were used according to manufacturer's recommendations.

**Immunofluorescence.** Tissue sections were processed as previously described (40). The procedure involved the tumor cell injection into mice and subsequent tissue fixation, decalcification, and cryo-sectioning of the mouse skeletal tissue to generate thick sections (60  $\mu$ m). Briefly, female Nod/SCID mice were injected via tail vein with Luc+/GFP+ MM.1S cells and monitored for 8 wk via BLI. Bones were harvested, fixed in 4% (wt/vol) PFA, and decalcified in ethylenediamine-tetraacetic acid for 24 h. The decalcified bones were embedded in gelatin and sucrose solution and frozen at -80 °C. The frozen tissue molds were placed in a precooled (-23 °C) cryostat and were sectioned at -23 °C. The thick sections (60  $\mu$ m) generated were stained as such: blood vessels with endomucin (red),

nuclei with DAPI (blue). MM.1S GFP+ cells are seen as green. The images were captured on Zeiss LSM 700 confocal and Zeiss LSM 710.

**Statistics.** All analyses were performed using GraphPad Prism 9 (La Jolla, CA) software; more specifically, statistical analysis was carried out with unpaired two-tailed t test or one- or two-way ANOVAs where appropriate. Data were plotted as mean  $\pm$  SD unless otherwise stated.

**Data, Materials, and Software Availability.** All study data are included in the article and/or *SI Appendix*.

**ACKNOWLEDGMENTS.** C.G.F.-E. was supported by a NSF Graduate Research Fellowship (DGE 1845298), a Graduate Education for Minorities Fellowship, a University of Pennsylvania Fontaine Fellowship, and the Hispanic Scholarship Fund. P.P.G.G. was supported by S. Leslie Misrock Cancer Nanotechnology Postdoctoral Fellowship. R.S.R. was supported by a NIH T32 multidisciplinary training grant (T32HL007954) and an NIH F32 postdoctoral fellowship (F32CA243475). C.L. was supported by an NIH K99/R00 (K99HL151670). S.J.S., R.M.H., and A.G.H. were supported by NSF Graduate Research Fellowships (DGE 1845298). M.J.M. acknowledges support from a Burroughs Wellcome Fund Career Award at the Scientific Interface, a US NIH Director's New Innovator Award (DP2TR002776), grants from the American Cancer Society (RSG-22-122-01-ET and 129784-IRG-16-188-38-IRG), an NSF CAREER Award (CBET-2145491), the NIH (R01CA241661, R37CA244911, and R01DK123049), and a 2018 AACR-Bayer Innovation and Discovery Grant, Grant Number 18-80-44-MITC. R.D.C. acknowledges support from the National Cancer Institute (NCI) (1R01CA248393, 1R01CA2123, and 1R01CA218549). This work was supported in part by the Koch Institute's Marble Center for Cancer Nanomedicine as well as the Bridge Project, a partnership between the Koch Institute for Integrative Cancer Research at MIT and the Dana Farber/Harvard Cancer Center. Resources were provided in part by the Koch Institute Cancer Center Support (core) grant P30-CA14051 from the NCI. The content is solely the responsibility of the authors and does not necessarily represent the official views of the NIH.

Author affiliations: <sup>a</sup>Department of Bioengineering, University of Pennsylvania, Philadelphia, PA 19104; <sup>b</sup>Department of Physiology and Biophysics, Institute of Biological Sciences, Universidade Federal de Minas Gerais, Belo Horizonte, MG 31270-901, Brazil; <sup>c</sup>Department of Biomedical Engineering, Rowan University, Glassboro, NJ 08028; <sup>d</sup>Department of Oncologic Pathology, Dana-Farber Cancer Institute, Harvard Medical School, Boston, MA 02215; <sup>e</sup>Department of Experimental Hematology, Institute of Hematology and Transfusion Medicine, Warsaw 02776, Poland; <sup>f</sup>Department of Materials Science & Engineering, University of Michigan, North Campus Research Complex, Ann Arbor, MI 48109; <sup>g</sup>David H. Koch Institute for Integrative Cancer Research, Massachusetts Institute of Technology, Cambridge, MA 02142; <sup>h</sup>Department of Bioengineering, Temple University, Philadelphia, PA 19122; <sup>i</sup>Department of Chemical Engineering, Massachusetts Institute of Technology, Cambridge, MA 02142; <sup>j</sup>Institute for Medical Engineering and Science, Massachusetts Institute of Technology, Cambridge, MA 02142; <sup>k</sup>Harvard and MIT Division of Health Science and Technology, Massachusetts Institute of Technology, Cambridge, MA 02142; <sup>l</sup>Department of Pathology, Brigham & Women's Hospital, Boston, MA 02115; <sup>m</sup>Abramson Cancer Center, Perelman School of Medicine, University of Pennsylvania, Philadelphia, PA 19104; <sup>n</sup>Institute for Immunology, Perelman School of Medicine, University of Pennsylvania, Philadelphia, PA 19104; <sup>o</sup>Cardiovascular Institute, Perelman School of Medicine, University of Pennsylvania, Philadelphia, PA 19104; and <sup>p</sup>Institute for Regenerative Medicine, Perelman School of Medicine, University of Pennsylvania, Philadelphia, PA 19104

Author contributions: P.P.G.G., C.G.F.-E., R.S.R., C.L., R.L., D.G.A., R.D.C., and M.J.M. designed research; P.P.G.G., C.G.F.-E., R.S.R., N.G., L.X., T.S., P.S.D., C.L., A.C., A.G.H., and R.E. performed research; P.P.G.G., C.G.F.-E., R.S.R., T.S., P.S.D., C.L., A.C., S.J.S., and M.J.M. contributed new reagents/analytic tools; P.P.G.G., C.G.F.-E., R.S.R., N.G., L.X., T.S., P.S.D., C.L., A.C., S.J.S., R.M.H., A.G.H., R.E., K.W., R.L., D.G.A., R.D.C., and M.J.M. analyzed data; and P.P.G.G., C.G.F.-E., R.S.R., S.J.S., R.M.H., K.W., R.L., D.G.A., R.D.C., and M.J.M. wrote the paper.

Competing interest statement: R.L. receives licensing fees (to patents in which he was an inventor on) from, invested in, consults (or was on Scientific Advisory Boards or Boards of Directors) for, lectured (and received a fee), or conducts sponsored research at MIT for which he was not paid for a large number of entities. A full list can be found in the *SI Appendix*. The other authors declare no competing interests.

1. R. L. Siegel, K. D. Miller, H. E. Fuchs, A. Jemal, Cancer statistics, 2021. *CA Cancer J. Clin.* **71**, 7–33 (2021).
2. S. K. Kumar *et al.*, Multiple myeloma. *Nat. Rev. Dis. Primers* **3**, 1–20 (2017).
3. A. Mahindra, T. Hideshima, K. C. Anderson, Multiple myeloma: Biology of the disease. *Blood Rev.* **24**, S5–S11 (2010).
4. J. Corre, N. Munshi, H. Avet-Loiseau, Genetics of multiple myeloma: Another heterogeneity level? *Blood* **125**, 1870–1876 (2015).
5. K. C. Anderson, Progress and paradigms in multiple myeloma. *Clin. Cancer Res.* **22**, 5419–5427 (2016).

6. W. M. Kuehl, P. L. Bergsagel, Molecular pathogenesis of multiple myeloma and its premalignant precursor. *J. Clin. Invest.* **122**, 3456–3463 (2012).
7. L. J. Costa *et al.*, Recent trends in multiple myeloma incidence and survival by age, race, and ethnicity in the United States. *Blood Adv.* **1**, 282–287 (2017).
8. A. Palumbo, K. Anderson, Multiple myeloma. *N. Engl. J. Med.* **364**, 1046–1060 (2011).
9. Y. C. Cohen *et al.*, Identification of resistance pathways and therapeutic targets in relapsed multiple myeloma patients through single-cell sequencing. *Nat. Med.* **27**, 491–503 (2021).
10. R. Eichner *et al.*, Immunomodulatory drugs disrupt the cereblon-CD147-MCT1 axis to exert antitumor activity and teratogenicity. *Nat. Med.* **22**, 735–743 (2016).

11. D. Ribatti, M. Moschetta, A. Vacca, Microenvironment and multiple myeloma spread. *Thromb. Res.* **133**, S102-S106 (2014).
12. Y. Kawano *et al.*, Targeting the bone marrow microenvironment in multiple myeloma. *Immunol. Rev.* **263**, 160-172 (2015).
13. C. S. Mitsiades, N. S. Mitsiades, N. C. Munshi, P. G. Richardson, K. C. Anderson, The role of the bone microenvironment in the pathophysiology and therapeutic management of multiple myeloma: Interplay of growth factors, their receptors and stromal interactions. *Eur. J. Cancer* **42**, 1564-1573 (2006).
14. R. Sklaventis-Pistofidis, M. Bustoros, I. M. Ghobrial, Bone marrow niche in multiple myeloma and its precursor states. *Hemisphere* **3**, 121-123 (2019).
15. Z. G. Jin *et al.*, Cyclophilin A is a proinflammatory cytokine that activates endothelial cells. *Arterioscler. Thromb. Vasc. Biol.* **24**, 1186-1191 (2004).
16. P. Nigro, G. Pompilio, M. C. Capogrossi, Cyclophilin A: A key player for human disease. *Cell Death Dis.* **4**, e888 (2013).
17. D. Zhu *et al.*, The Cyclophilin A-CD147 complex promotes the proliferation and homing of multiple myeloma cells. *Nat. Med.* **21**, 572-580 (2015).
18. E. de Bruyne *et al.*, Myeloma cells and their interactions with the bone marrow endothelial cells. *Curr. Immunol. Rev.* **3**, 41-55 (2007).
19. R. Ria *et al.*, Gene expression profiling of bone marrow endothelial cells in patients with multiple myeloma. *Clin. Cancer Res.* **15**, 5369-5378 (2009).
20. D. Ribatti, B. Nico, A. Vacca, Importance of the bone marrow microenvironment in inducing the angiogenic response in multiple myeloma. *Oncogene* **25**, 4257-4266 (2006).
21. J. E. Dahlman *et al.*, In vivo endothelial siRNA delivery using polymeric nanoparticles with low molecular weight. *Nat. Nanotechnol.* **9**, 648-655 (2014).
22. M. Krohn-Grimberghe *et al.*, Nanoparticle-encapsulated siRNAs for gene silencing in the haematopoietic stem-cell niche. *Nat. Biomed. Eng.* **4**, 1076-1089 (2020).
23. C. D. Sago *et al.*, Nanoparticles that deliver RNA to bone marrow identified by in vivo directed evolution. *J. Am. Chem. Soc.* **140**, 17095-17105 (2018).
24. M. A. Oberli *et al.*, Lipid nanoparticle assisted mRNA delivery for potent cancer immunotherapy. *Nano Lett.* **17**, 1326-1335 (2017).
25. J. E. Dahlman *et al.*, Barcoded nanoparticles for high throughput in vivo discovery of targeted therapeutics. *Proc. Natl. Acad. Sci. U.S.A.* **114**, 2060-2065 (2017).
26. K. T. Love *et al.*, Lipid-like materials for low-dose, in vivo gene silencing. *Proc. Natl. Acad. Sci. U.S.A.* **107**, 1864-1869 (2010).
27. K. A. Hajj *et al.*, Branched-tail lipid nanoparticles potently deliver mRNA in vivo due to enhanced ionization at endosomal pH. *Small* **15**, 1-7 (2019).
28. H. Y. Cheng, L. J. Lai, F. H. Ko, Rapid and sensitive detection of rare cancer cells by the coupling of immunomagnetic nanoparticle separation with ELISA analysis. *Int. J. Nanomed.* **7**, 2967-2973 (2012).
29. P. P. G. Guimaraes *et al.*, Ionizable lipid nanoparticles encapsulating barcoded mRNA for accelerated in vivo delivery screening. *J. Controlled Release* **316**, 404-417 (2019).
30. D. Chen *et al.*, Rapid discovery of potent siRNA-containing lipid nanoparticles enabled by controlled microfluidic formulation. *J. Am. Chem. Soc.* **134**, 6948-6951 (2012).
31. K. Paunovska *et al.*, A direct comparison of in vitro and in vivo nucleic acid delivery mediated by hundreds of nanoparticles reveals a weak correlation. *Nano Lett.* **18**, 2148-2157 (2018).
32. C. Xue *et al.*, Endothelial-to-mesenchymal transition and inflammation play key roles in Cyclophilin A-induced pulmonary arterial hypertension. *Hypertension* **76**, 1113-1123 (2020).
33. X. Wang *et al.*, The effect of honokiol on pulmonary artery endothelium cell autophagy mediated by cyclophilin A in hypoxic pulmonary arterial hypertension. *J. Pharmacol. Sci.* **139**, 158-165 (2019).
34. X. Jiang, Q. L. Zhang, Y. H. Tian, J. C. Huang, G. L. Ma, RNA interference-mediated gene silencing of cyclophilin A enhances the radiosensitivity of PAa human lung adenocarcinoma cells in vitro. *Oncol. Lett.* **13**, 1619-1624 (2017).
35. R. S. Riley, C. H. June, R. Langer, M. J. Mitchell, Delivery technologies for cancer immunotherapy. *Nat. Rev. Drug Discov.* **18**, 175-196 (2019).
36. M. M. Billingsley *et al.*, Ionizable lipid nanoparticle-mediated mRNA delivery for human CART cell engineering. *Nano Lett.* **20**, 1578-1589 (2020).
37. X. Zhao, C. Zhang, X. Cui, Y. Liang, "Interactions of hematopoietic stem cells with bone marrow niche" in *Methods in Molecular Biology* (Humana Press Inc., pp. 21-34. 2021).
38. P. M. L. Rood, J. Calafat, A. E. G. K. von dem Borne, W. R. Gerritsen, C. E. van der Schoot, Immortalisation of human bone marrow endothelial cells: Characterisation of new cell lines. *Eur. J. Clin. Invest.* **30**, 618-629 (2000).
39. M. Mani *et al.*, BCL9 promotes tumor progression by conferring enhanced proliferative, metastatic, and angiogenic properties to cancer cells. *Cancer Res.* **69**, 7577-7587 (2009).
40. A. P. Kusumbe, S. K. Ramasamy, A. Starsichova, R. H. Adams, Sample preparation for high-resolution 3D confocal imaging of mouse skeletal tissue. *Nat. Protoc.* **10**, 1904-1914 (2015).